RECONSTRUCTION OF HIGH-CURVATURE FREE-FORM SURFACES FROM REVERSE ENGINEERING DATA USING CURVATURE FIELD ANALYSIS AND VARIATIONAL OPTIMIZATION

Thien Nguyen Van[1], Dung Le Van[1], Phan Nguyen Huu[1,*], Minh Dao Binh[1], Hung Do Duy[1]

DOI: https://doi.org/10.57001/huih5804.2026.125

ABSTRACT

Reverse engineering (RE) has become a key technological solution in modern product design and development, particularly for industries involving complex free-form geometries such as automotive, aerospace, and mold manufacturing. However, reconstructing free-form surfaces with high curvature, complex boundaries, and stringent requirements on geometric smoothness and optical surface quality remains a significant challenge in practical applications. This paper proposes a novel method for high-curvature free-form surface reconstruction from reverse engineering data by integrating curvature field analysis with variational optimization. The proposed approach addresses three major challenges: (1) optimal surface patch layout determination through Gaussian curvature field analysis; (2) reconstruction of base curve networks with an optimal balance between data fidelity and geometric smoothness using a variational formulation; and (3) generation of the final surface using tensor-product Bézier surface modeling with enforced G^2 continuity constraints. The proposed method is validated using 3D scanned data of a complex automotive surface, specifically a rear bumper of a Porsche Macan. Experimental results demonstrate that the reconstructed surface exhibits superior geometric quality and high technical accuracy, with a mean deviation of 0.087mm. Moreover, full G^2 continuity is consistently maintained across patch boundaries, resulting in smooth curvature transitions and stable optical reflection behavior. These results confirm the effectiveness of the proposed method for reconstructing complex free-form surfaces that satisfy both stringent engineering accuracy requirements and high aesthetic quality standards. Future research will focus on extending this framework to surfaces with more complex topological structures and exploring the integration of deep learning-based point cloud segmentation to further automate the surface reconstruction pipeline.

Keywords: *CAS; Reverse Engineering; Bézier Surface; High-Quality Free-Form Surface Reconstruction*; *Curvature Field Analysis; Variational Optimization.*

[1]Hanoi University of Industry, Vietnam
[*]Email: nguyenhuuphan@haui.edu.vn

Received: 28/02/2026
Revised: 07/5/2026
Accepted: 25/5/2026

1. INTRODUCTION

In recent years, reverse engineering (RE) has become an increasingly important approach in product research and development, particularly for the geometric reconstruction of components with complex shapes [1, 11]. However, the reconstruction of free-form surfaces with stringent requirements on geometric quality and continuity remains a significant challenge for existing methods, especially in surface design applications demanding high levels of geometric smoothness and optical quality [2, 9].

One of the fundamental difficulties in free-form surface reconstruction originates from the nature of the input data. Data acquired from 3D scanning systems typically exist in the form of discrete point clouds or triangular meshes, which are inherently affected by measurement noise and do not intrinsically possess geometric continuity properties such as G^0, G^1, or G^2 [1, 15, 16]. In contrast, these levels of geometric continuity play a crucial role in the characterization and control of high-quality free-form surfaces, particularly in Class-A surface design [9, 10]. Consequently, direct fitting methods based on raw scan data, if not accompanied by appropriate smoothing mechanisms and curvature control strategies, often lead to local curvature oscillations and a degradation of the overall geometric quality of the reconstructed surface [1, 5].

In addition to data-related issues, many existing surface reconstruction workflows still rely heavily on the subjective experience of designers. The determination of patch layouts and surface structures is often performed through manual operations or experience-based heuristics, lacking clear quantitative criteria for controlling curvature fields and higher-order surface

derivatives [6, 7]. As a result, achieving second-order geometric continuity (G^2) across patch boundaries in a consistent manner remains difficult, and in many cases, only tangent continuity (G^1) is attained [3, 12].

Recent advances in differential geometry have provided important theoretical foundations for improving the geometric quality of reconstructed surfaces. Tsuchie et al. [3] demonstrated that geodesics and lines of curvature can be exploited as guiding geometric features in surface reconstruction, thereby enhancing geometric continuity and reducing undesirable curvature fluctuations. In parallel, partial differential equation (PDE)-based surface reconstruction methods have shown strong potential for automating surface smoothing while enabling the construction of G^2-continuous surfaces under appropriate boundary conditions, without excessively compromising adherence to the input scan data [4, 17].

From an application perspective, several studies have employed commercial and semi-automatic reverse engineering platforms, such as Geomagic Design X and Geomagic Studio, to reconstruct complex free-form surfaces from 3D scan data [6, 7]. These workflows facilitate efficient feature extraction and surface fitting, as well as the creation of editable CAD models, and have been successfully applied in styling design and clay modeling practices [13, 14]. Nevertheless, such workflows still largely depend on user interaction and lack tight integration with quantitative geometric criteria, particularly for global curvature continuity control. As a consequence, G^2 continuity is often achieved only locally rather than across the entire surface [6, 7].

Motivated by the above limitations, this study proposes an integrated methodological framework that combines differential geometry and variational optimization to enhance geometric quality control in reverse engineering. By exploiting the Gaussian curvature field to assist in patch layout determination and by formulating an energy function that balances data fidelity and geometric smoothness (regularization), the proposed approach aims to automate surface smoothing and improve the robustness of achieving G^2 continuity across patch boundaries.

2. RESEARCH METHODS

2.1. Data Measurement and Acquisition

To evaluate the effectiveness and robustness of the proposed surface reconstruction method based on Gaussian curvature field analysis combined with variational optimization, an automotive rear bumper component (Figure 1) was selected as the experimental case study. This geometry is highly representative of complex free-form surfaces, as it exhibits pronounced curvature variations along both parametric directions, the presence of sharp character lines with small radii of curvature, and extensive transition regions that require stringent control of higher-order geometric continuity.

Figure 1. Photograph of the actual automotive rear bumper component

Data Acquisition and Preprocessing Workflow

The input data were acquired using a structured white-light optical 3D scanning system with a spatial resolution of 0.05mm and an accuracy of ±0.03mm. The physical dimensions of the scanned component are 647 × 963 × 647mm. To ensure comprehensive surface coverage and data consistency, the scanning process was performed on an automated rotary table under controlled lighting conditions. The data acquisition and preprocessing operations were carried out using Creaform VXelements software for point cloud capture and initial processing. Subsequent mesh repair, noise filtering, and STL format conversion were performed using Geomagic Design X (3D Systems).

The raw scanning data were subsequently subjected to a standard preprocessing pipeline, including the following steps:

Coarse noise removal: Elimination of outlier points caused by light reflection artifacts and background noise.

Point cloud registration and merging: Alignment and integration of multiple scans acquired from different viewing angles into a unified global coordinate system.

Remeshing: Conversion of the merged point cloud into a uniform polygonal (triangular) mesh structure.

As a result of this preprocessing workflow, a high-quality triangular mesh satisfying the necessary conditions for subsequent experimental analysis was

obtained (Figure 2). The detailed scanning parameters and mesh characteristics of the acquired dataset are summarized in Table 1.

Table 1. Characteristic parameters of the scanned rear bumper dataset

Parameter	Value
Number of vertices	60,660 (V)
Number of triangular faces	104,630 (F)
Data representation	Discrete triangular mesh
Scanning method	Structured-light optical 3D scanning
Scanning device	Creaform HandySCAN 3D
Scan resolution	0.05mm
Scan accuracy	± 0.03mm
Bounding dimensions	647 × 963 × 647mm
Input file format	STL
Noise characteristics	Local high-frequency noise

Figure 2. Point cloud data of the rear bumper component used as the experimental case study

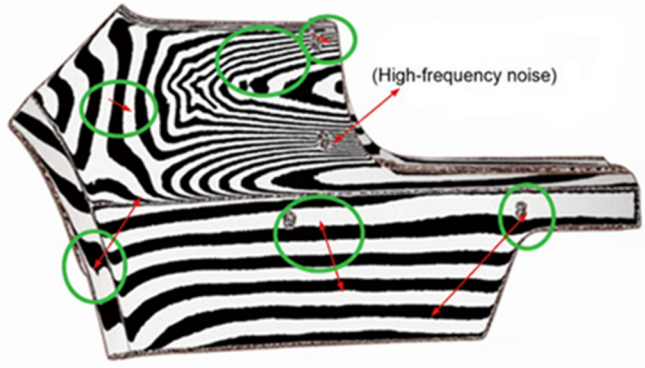

Figure 3. Zebra striping analysis on the preprocessed mesh data

The circled regions in Figure 3 illustrate the presence of high-frequency noise and jagged artifacts, which disrupt the geometric continuity of the surface. The occurrence of such noise on a surface with highly varying curvature provides a practical basis for evaluating the proposed reconstruction algorithm.

One of the major challenges in this problem lies in achieving an appropriate balance between noise suppression and geometric fidelity. Conventional smoothing techniques often result in over-smoothing, leading to surface shrinkage or the loss of the designer's original intent.

In contrast, the proposed variational optimization approach guided by the Gaussian curvature field aims to address these two competing objectives simultaneously:

Effective noise suppression: High-frequency ripples and jagged artifacts are eliminated through surface energy minimization, thereby ensuring improved geometric continuity.

Preservation of the original data: By employing the intrinsic curvature field as a control parameter, the denoising process becomes directionally adaptive. This allows the algorithm to selectively act on local deviations without altering the global surface structure, ensuring close adherence to the original point cloud, particularly in regions of high curvature and along sharp character lines.

This curvature-guided denoising strategy constitutes a key advantage of the proposed method, enabling an optimal balance between aesthetic smoothness and engineering accuracy, while preserving the mechanical fidelity of the original physical component.

2.2. Data processing methodology

This section is restructured into three components: (i) curvature field-based surface segmentation (Section 2.2.1); (ii) variational construction of base-curve networks (Section 2.2.2); and (iii) primary and transition surface construction via variational optimization (Sections 2.2.3 - 2.2.4).

2.2.1. Surface segmentation based on curvature field

To support the surface segmentation stage in the reconstruction process, this study employs fundamental concepts from differential geometry to accurately characterize the local curvature structure of the surface [12].

Gauss map:

For a regular surface $S \subset \mathbb{R}^3$, the Gauss map is defined as:

$$N: S \to S2, p \mapsto n(p) \quad (1)$$

which assigns to each point $p$on the surface a unit normal vector on the unit sphere $\mathbb{S}^2$.

The differential of the Gauss map at point p,

$$dN_p: T_p(S) \to T_p(S) \quad (2)$$

is a self-adjoint linear operator that plays a central role in describing the local curvature behavior of the surface.

Second fundamental form

The second fundamental form at point p is defined as:

$$\Pi_p(v) = -\langle dN_p(v), v\rangle, v \in T_p(S) \quad (3)$$

which characterizes the extent to which the surface deviates from its tangent plane along direction

Principal curvatures and principal directions

At each point p, there exists an orthonormal basis $\{e_1, e_2\}$ such that:

$$dN_p(e_1) = -k_1 e_1, dN_p(e_2) = -k_2 e_2 \quad (4)$$

where k_1 and k_2 denote the maximum and minimum principal curvatures at the given point, respectively. The associated eigenvectors e_1 and e_2, referred to as the principal directions, characterize the dominant curvature directions and serve as geometric guides in the surface segmentation process.

Gaussian and mean curvatures

From the eigenvalues of the differential of the Gauss map dN_p, two fundamental intrinsic geometric invariants are defined:

$$K = \det(dN_p) = k_1 k_2 \quad (5)$$

$$K = det(dN_p) = k_1 k_2 \quad (6)$$

$$H = -\frac{1}{2} trace(dN_p) = \frac{k_1 + k_2}{2} \quad (7)$$

These quantities characterize the overall curvature behavior of the surface and serve as key descriptors for morphology-based surface segmentation.

Surface point classification based on gaussian curvature

The sign of the Gaussian curvature K allows the geometric nature of each surface point to be classified as follows:

Point Type	Condition	Geometric Characteristics
Elliptic	$K > 0$	Locally convex or concave surface; principal curvatures have the same sign (Figure 4a)
Hyperbolic	$K < 0$	Saddle-shaped surface; principal curvatures have opposite signs (Figure 4b)
Parabolic	$K \approx 0$, Np $\neq 0$	One principal curvature is approximately zero (Figure 4c)

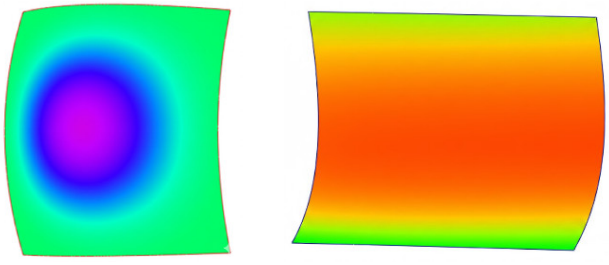

a) positive b) negative

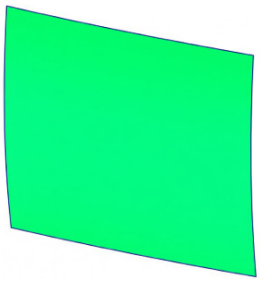

c) zero

Figure 4. Types of Gaussian Curvatures a) positive, b) negative and c) zero

2.2.2. Geometric continuity and variational construction of base-curve networks

In computational geometric design and free-form surface reconstruction from scanned data, geometric continuity plays a pivotal role in ensuring geometric smoothness, curvature-field stability, and optical consistency at junctions between curves and surface patches [9]. These continuity levels describe the compatibility of positional, tangential, and curvature-related properties, and they directly affect the overall geometric quality of the reconstructed surface.

a) Geometric continuity of curves

In this study, $C^1$and C^2continuity conditions are enforced through linear constraints on Bézier control points, following standard formulations in parametric curve design.

Given two parametric curves $C_1(t)$ and $C_2(t)$, geometric continuity is defined at four levels as follows:

G0 (Point Continuity): The two curves meet at a common point. Their positions coincide, but their tangent directions may be discontinuous.

$$C_1(t_1) = C_2(t_2) \quad (8)$$

G1 (Tangent Continuity): The curves share a common point and have aligned tangent directions at the junction, producing a visually smoother transition than G^0.

$$C_1'(t_1) \parallel C_2'(t_2) \quad (9)$$

G2 (Curvature Continuity): In addition to position and tangent continuity, the two curves also share identical curvature at the junction point, resulting in a highly smooth transition without abrupt curvature changes. The four levels of geometric continuity described above are illustrated in Figure 5.

$$C1''(t1) \parallel C2''(t2) \quad (10)$$

For curves composed of multiple segments, geometric continuity at junction points is mandatory to ensure smooth transitions. Specifically, two curve

segments $P[t_0, t_1]$ and $Q[t_1, t_2]$ are said to be C^k-continuous (parametric continuity of order k) at the junction t_1 if the following conditions are satisfied [9]:

$$P(t_1) = Q(t_1), P'(t_1) = Q'(t_1), \ldots,$$
$$P^k(t_1) = Q^k(t_1) \quad (11)$$

where $P^{(k)}(t_1)$ denotes the k-th derivative of curve P at t_1. These derivatives must coincide in both magnitude and direction.

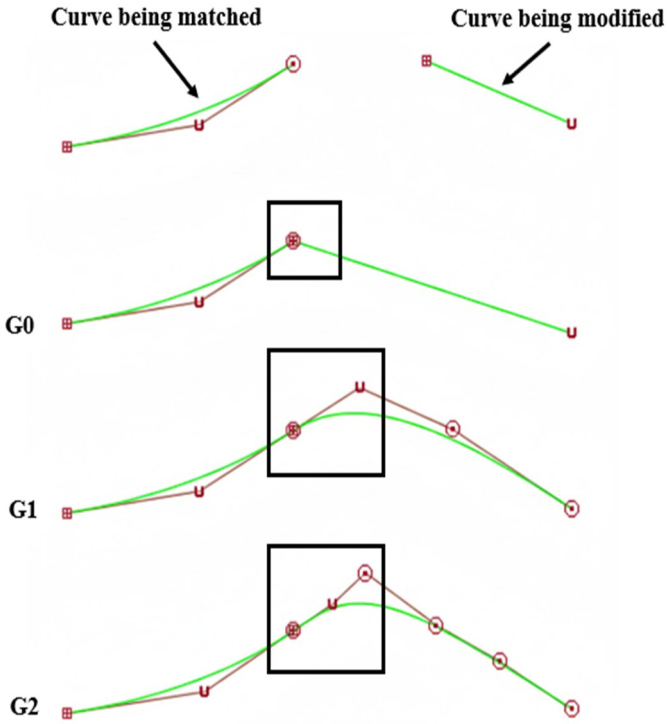

Figure 5. Levels of geometric continuity for curves

b) Base-curve network for high-quality surface reconstruction

In high-quality surface design, the base-curve network serves as the geometric backbone governing the topological structure and overall surface quality. An inadequately controlled curve network may lead to patch distortion, loss of geometric continuity at patch boundaries, and optical artifacts in reflective regions.

Inspired by Tsuchie's methodology exploiting geodesic flows and lines of curvature in surface reconstruction [3], this study develops a two-stage procedure for base-curve network construction:

Extraction of coarse boundary curves from scanned data.

Reconstruction of Bézier curves using a variational optimization framework with differential-geometric constraints, ensuring smoothness and curvature alignment with the intrinsic surface structure.

The extracted raw curves often contain high-frequency "saw-tooth" noise. To restore Class-A quality curves, a variational optimization model is applied, in which each Bézier curve $C(t)$ is constrained to follow two fundamental surface-flow principles [3].

Principle P1 - Geodesic approximation constraint (Φ):

The curve is treated as an "ideal measuring curve" that follows the shortest path on the surface, minimizing bending energy:

$$\Phi\big(C(t)\big) = -\Gamma^u_{vv}\frac{G}{\sqrt{EG-F^2}} \approx 0 \quad (12)$$

where Γ^u_v denotes the Christoffel symbols of the second kind. This constraint limits lateral deviation and encourages the curve to adhere to the global surface shape.

Principle P2 - Line-of-curvature approximation constraint (Ψ)

To reduce intrinsic torsion and ensure alignment with the natural curvature directions of the surface, the following constraint is imposed:

$$\Psi\big(C(t)\big) = (FN - GM)\, dt^2 \approx 0 \quad (13)$$

where (E, F, G) and (L, M, N) are the coefficients of the first and second fundamental forms, respectively.

Together, constraints Φ and Ψ form a geometric backbone, ensuring that curves follow the curvature flow of the surface and thereby reducing distortion during subsequent surface construction.

Optimal Energy Functional for Bézier Curve Reconstruction:

Each bézier curve $C(t)$ is determined by minimizing the following energy functional:

$$J = \epsilon_0 \sum_{i=1}^{M} \| C(t_i) - Q_i \|^2 + \epsilon_1 \sum_{k=1}^{N} | \mathcal{L}(C) |^2$$
$$+\epsilon_2 \sum_{k=1}^{N} | \Phi(C) |^2 + \epsilon_3 \sum_{k=1}^{N} | \Psi(C) |^2 \quad (14)$$

where:

- Fitting Accuracy (ε_0) preserves the global shape derived from scanned data

- Fairing Term (ε_1) controls second-order curvature variation via the operator $L(C)$, ensuring monotonic curvature combs - a key criterion for Class-A curves

- Geodesic and Line-of-Curvature Constraints ($\varepsilon_2, \varepsilon_3$) maintain curvature direction consistency and geometric harmony

The resulting constrained least-squares optimization yields Bézier control points that define geometrically stable curves suitable for the subsequent variational surface reconstruction stage, without imposing explicit industrial styling heuristics.

2.2.3. Primary surface creation

After establishing the topological wireframe from geometric segmentation, the next stage involves constructing primary surface patches, which serve as foundational geometric domains for continuous surface reconstruction. The objective of this stage is to generate surface regions with stable mathematical representations, sufficient smoothness order, and controllable geometric degrees of freedom for subsequent optimization.

Tensor-product bézier surface representation

Each surface patch $S_j$is defined as a two-parameter mapping:

$S_j: [0,1]^2 \rightarrow \mathbb{R}^3$,

bounded by four boundary curves $\{c_a, c_b, c_c, c_d\}$ (Figure 6):

$$S_j(u,0) = c_a(u), S_j(u,1) = c_b(u) \quad (15)$$

$$S_j(0,v) = c_c(v), S_j(1,v) = c_d(v) \quad (16)$$

To ensure geometric stability and differential controllability, a tensor-product Bézier representation of degree (p, q) is employed (Figure 7):

$$S_j(u,v) = \sum_{m=0}^{p} \sum_{n=0}^{q} P_{m,n}. B_m^p(u). B_n^q(v) \quad (17)$$

where $P_{m,n}$ denotes the control-point grid and $B_k^n(\cdot)$ are Bernstein polynomials. The control-point lattice $P_{m,n}$ acts as the optimization variable, directly governing the surface geometry and curvature characteristics (Figure 7).

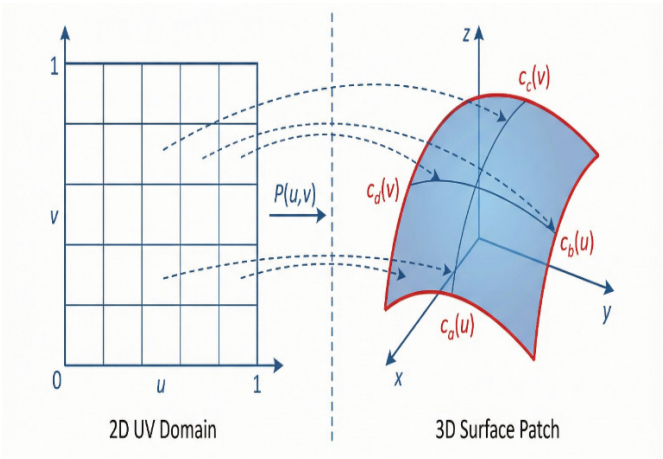

Figure 6. Parametric mapping from the (u, v)domain to 3D space, bounded by boundary curves

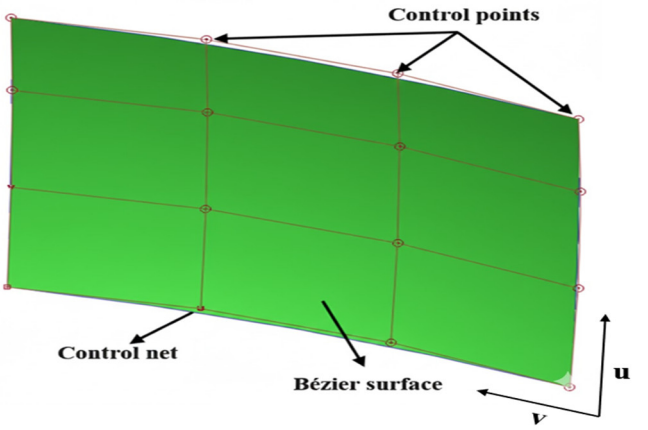

Figure 7. Tensor-product Bézier surface controlled by the control-point network $P_{m,n}$

Initialization of the Control Mesh Using Coons Interpolation

The initialization stage plays a critical role in avoiding poor local minima and accelerating convergence of the optimization process. A two-level strategy is adopted: The resulting initialized control mesh is illustrated in Figure 8.

(1) Boundary control point initialization. The boundary rows and columns of control points $\{P_{m,0}, P_{m,q}, P_{0,n}, P_{p,n}\}$ are assigned by uniformly sampling the corresponding boundary curves in the parametric domain. This ensures strict C^0geometric compatibility between adjacent surface patches from the very beginning of the process.

(2) Interior control point interpolation via bilinear Coons formulation. Interior control points $P_{m,n}$ (with $0 < m < p$, $0 < n < q$) are interpolated using a simplified Coons bilinear scheme:

$$P_{m,n} = (1 - v_n)P_{m,0} + v_n P_{m,q} + (1 - u_m)P_{0,n} + u_m P_{p,n} - P_{m,n}^{\text{bilinear}} \quad (18)$$

where $P_{m,n}^{\text{bilinear}}$ represents the bilinear correction term that removes duplicated corner contributions. This procedure yields a well-formed control mesh with a reasonable curvature distribution, providing a stable starting point for subsequent variational optimization.

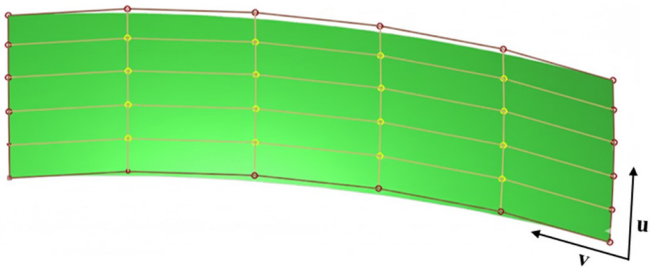

Figure 8. Control mesh initialized using Coons interpolation: boundary control points (red) are fixed, interior points (yellow) are bilinearly interpolated

Multi-objective variational optimization

Although the initialized surface is sufficiently smooth, its geometric fidelity to the scanned data is not yet guaranteed. Therefore, the control mesh is refined by minimizing composite energy functional [4, 5]:

$$E(P) = \alpha E_{\text{fit}} + \beta E_{\text{smooth}} \quad (19)$$

where:

Data fitting energy:

$$E_{\text{fit}} = \sum_k \omega_k \parallel S(u_k, v_k) - D_k \parallel^2 \quad (20)$$

This term penalizes the deviation between the surface and the scanned data points $\{D_k\}$, with adaptive weights ω_k emphasizing geometrically significant regions.

Thin-plate smoothing energy:

$$E_{\text{smooth}} = \iint_\Omega (\parallel S_{uu} \parallel^2 + 2 \parallel S_{uv} \parallel^2 + \parallel S_{vv} \parallel^2)\, du\, dv \quad (21)$$

This regularization term suppresses high-frequency oscillations and drives the surface toward a minimum bending-energy state - an essential characteristic of Class-A surfaces.

Optimization algorithm. A flowchart illustrating the complete iterative algorithm including initialization via Coons interpolation, L-BFGS update steps, and convergence checking criteria should be added here to enhance the reproducibility and clarity of the proposed methodology.

The problem:

$$\min_{P_{m,n}} E(P) \quad (22)$$

is convex with respect to the control points when the parameters (u_k, v_k) are fixed. The L-BFGS algorithm is employed due to its fast convergence and low memory requirements.

2.2.4. Transition surface construction and geometric continuity constraints

Surface continuity levels

For two parametric surfaces $S_1(u, v)$ and $S_2(u, v)$ sharing a common boundary, three commonly used continuity levels are defined [9]:

G0 (Position continuity): The surfaces meet at the boundary with coincident positions only, resulting in a sharp edge or corner (Figure 9).

G1 (Tangent continuity): Both position and tangent directions are continuous across the boundary. The transition appears visually smooth, although reflection analysis may still reveal a seem (Figure 10).

G2 (Curvature continuity): Position, tangents, and curvature are all continuous across the boundary, producing a seamless transition that remains indistinguishable even under reflection inspection (Figure 11).

Similar to curve design, G2 continuity is mandatory for visible surfaces in automotive and high-end consumer products, as it guarantees uninterrupted light reflection and superior optical quality.

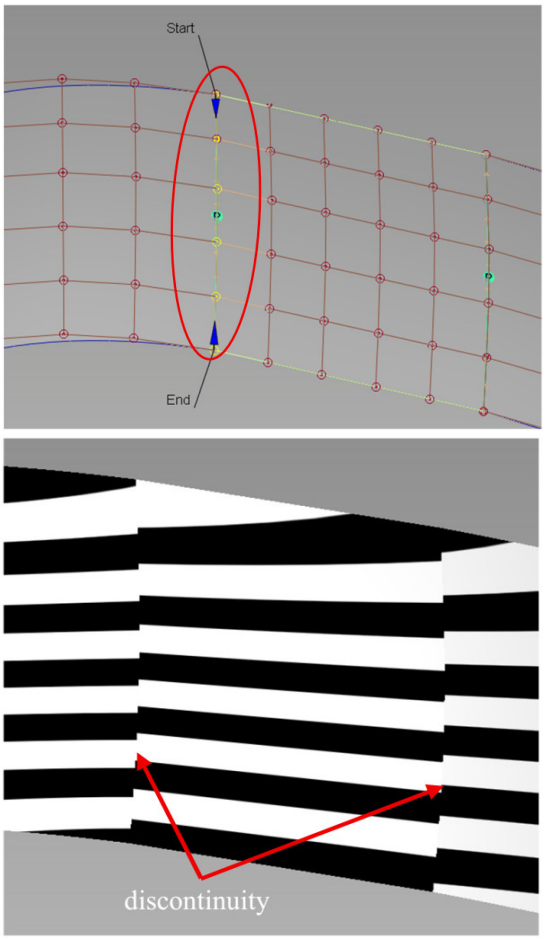

Figure 9. Illustration of G0 continuity between two surfaces (left) and reflection inspection using Zebra analysis (right)

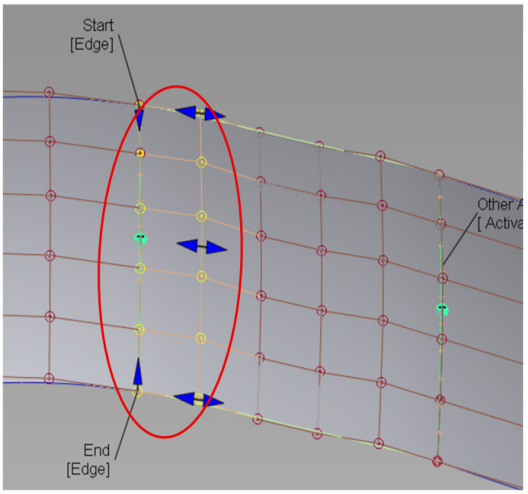

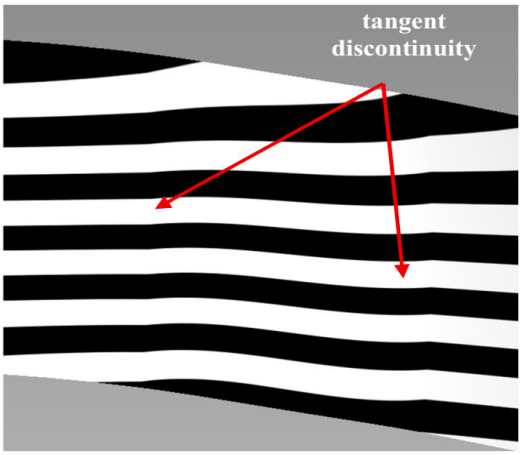

Figure 10. Illustration of G1 continuity between two surfaces (left) and reflection inspection using Zebra analysis (right)

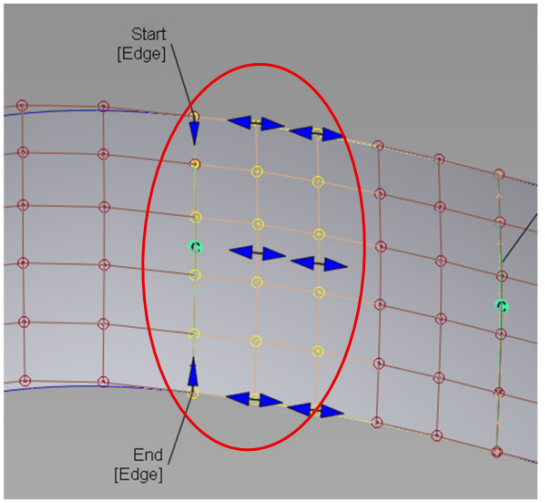

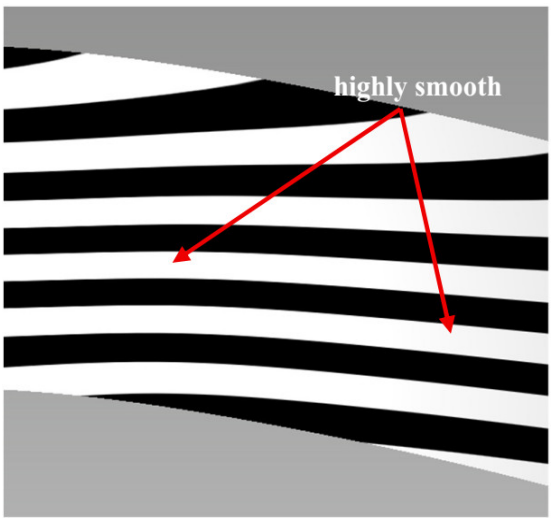

Figure 11. Illustration of G2 continuity between two surfaces (left) and reflection inspection using Zebra analysis (right)

G^2 boundary continuity conditions

Consider a transition surface $S_2(u,v)$ smoothly joined to a primary surface $S_1(u,v)$ along the common boundary $u = 0$. Second-order geometric continuity (G^2) requires not only positional and tangent continuity but also full compatibility of the normal curvature and the variation of surface normals along the shared boundary.

The G^2 continuity condition can be formalized through the following partial derivative relationship:

$$\frac{\partial^2 S_2}{\partial u^2} = \alpha(v)\left(\frac{\partial S_1}{\partial u}\right)^2 + \beta(v)\frac{\partial^2 S_1}{\partial u^2} + \gamma(v)\frac{\partial S_1}{\partial u} \quad (23)$$

where the scalar functions $\alpha(v)$, $\beta(v)$, and $\gamma(v)$ regulate the parametric scaling and the normal orientation along the joining boundary. These functions play a critical role in enforcing both first-order (G^1) and second-order (G^2) geometric continuity between the transition surface and the primary surface.

By satisfying these constraints, the surface connection avoids common Class-A defects such as reflection breaks, torsional distortions, and abrupt variations in the curvature field artifacts that are particularly visible under highlight line or zebra analysis. During optimization, the second and third rows of control points are allowed to move freely to satisfy the G^2 conditions, while the boundary control points are directly constrained to the primary surface S_1 to preserve geometric stability. The optimization framework is therefore designed to simultaneously minimize fitting error with respect to the scanned data and enforce G^2 continuity, resulting in a transition surface that is both geometrically accurate and optically smooth.

Optimization functional

To ensure both (i) data fidelity and (ii) G^2 geometric continuity, the following objective functional is minimized:

$$J(S_{\text{trans}}) = w_1 \iint_{\Omega} \| S_{\text{trans}}(u,v) - D_{\text{scan}}(u,v) \|^2 \, du\, dv + w_2 \int_{\Gamma} \| \kappa_2(s) - \kappa_1(s) \|^2 \, ds \quad (24)$$

where w_1 and w_2 are weighting coefficients balancing the trade-off between data fitting accuracy and curvature smoothness. Here, Ω denotes the scanned data domain, Γrepresents the shared boundary between the two surfaces, and κ_1 and κ_2 are the normal curvatures of the primary and transition surfaces evaluated along Γ, respectively.

The optimization is performed iteratively using a gradient descent scheme, in which the Bézier control points P_{ij} are updated as:

$$P_{ij}^{(k+1)} = P_{ij}^{(k)} - \eta \frac{\partial J}{\partial P_{ij}} \quad (25)$$

where η is the learning rate and $\frac{\partial J}{\partial P_{ij}}$ denotes the gradient of the objective functional with respect to the

control point P_{ij}. These gradients are computed using the partial derivatives of the Bézier surface:

$$\frac{\partial S}{\partial u} = \sum P_{ij} \frac{dB_i^n}{du} B_j^m(v), \frac{\partial^2 S}{\partial u^2} = \sum P_{ij} \frac{d^2 B_i^n}{du^2} B_j^m(v) \quad (26)$$

The iterative process terminates when both convergence criteria are satisfied:

$$\| \kappa_2 - \kappa_1 \| < \varepsilon \text{và} \| \Delta P \| < \tau \quad (27)$$

Indicating that curvature mismatch along the boundary and control point displacement have fallen below predefined thresholds. At this stage, the transition surface is considered converged and meets the required geometric and optical quality.

3. RESULTS AND DISCUSSION

3.1. Patch layout derived from gaussian curvature field analysis

In the early stage of the surface reconstruction pipeline, establishing an appropriate patch layout is a critical preprocessing step aimed at decomposing the geometry into subregions exhibiting homogeneous geometric behavior. Unlike conventional workflows that rely heavily on subjective designer experience, this study constructs the patch layout through a quantitative procedure grounded in differential geometry theory and the morphological characteristics of the automotive rear bumper geometry (Figure 12).

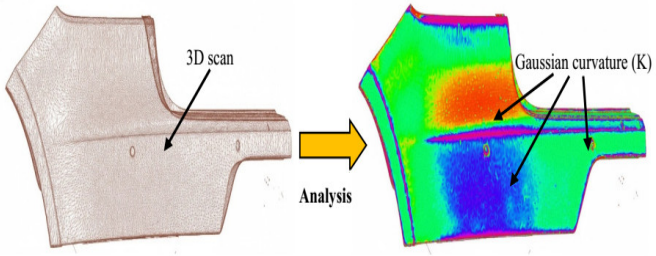

Figure 12. Gaussian curvature analysis for surface reconstruction of the rear bumper from 3D scanned data

Based on the Gaussian curvature K and mean curvature values computed at each surface point, a curvature feature space is established. This feature space directly reflects the intrinsic morphological regions of the surface, including elliptic, hyperbolic, parabolic, and near-planar areas. These curvature regimes represent fundamental geometric behaviors commonly observed in complex free-form surfaces and can be systematically classified according to the sign and magnitude of the curvature measures [3, 12]. Rather than redefining geometric concepts, the proposed approach directly leverages this curvature feature space to guide the surface partitioning process.

The surface is subsequently segmented using unsupervised clustering algorithms operating in the curvature feature space, such as *k-means*, *mean shift*, or *spectral clustering*. Importantly, the clustering is performed not on pure geometric coordinates but on curvature similarity, enabling the grouping of points with consistent geometric behavior. Each resulting cluster is treated as a candidate region for Bézier patch construction: elliptic clusters ($K > 0$) correspond to locally convex or concave stable regions; hyperbolic clusters ($K < 0$) identify transition areas with saddle-like behavior; while parabolic ($K \approx 0$) or near-planar clusters provide suitable domains for patches with simpler geometric structure.

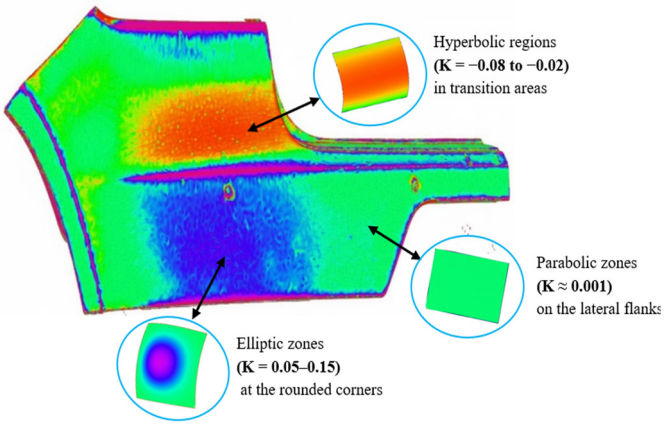

Figure 13. Gaussian curvature distribution and corresponding surface segmentation results

Figure 13 illustrates the Gaussian curvature distribution and the resulting segmentation. Defining the patch layout in this curvature-driven manner allows patch boundaries to align naturally with the intrinsic morphological transitions of the surface. This significantly facilitates subsequent Bézier fitting and optimization stages while reducing the risk of curvature discontinuities and visual artifacts along patch boundaries.

3.2. Evaluation of curve reconstruction efficienc

From each sectional curve directly extracted from the scanned data which is inherently affected by measurement noise and exhibits significant fluctuations in the curvature field the proposed variational optimization framework enables the transformation of the initial raw curve into a set of geometrically stable single Bézier segments. After optimization, the curve is represented by a sequence of low-degree Bézier segments, in which curvature varies smoothly and continuously along the entire arc length, while high-frequency oscillations are effectively suppressed.

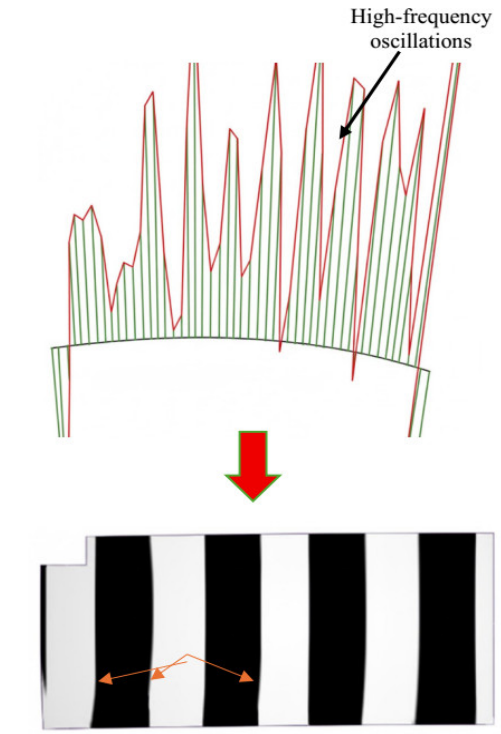

a)

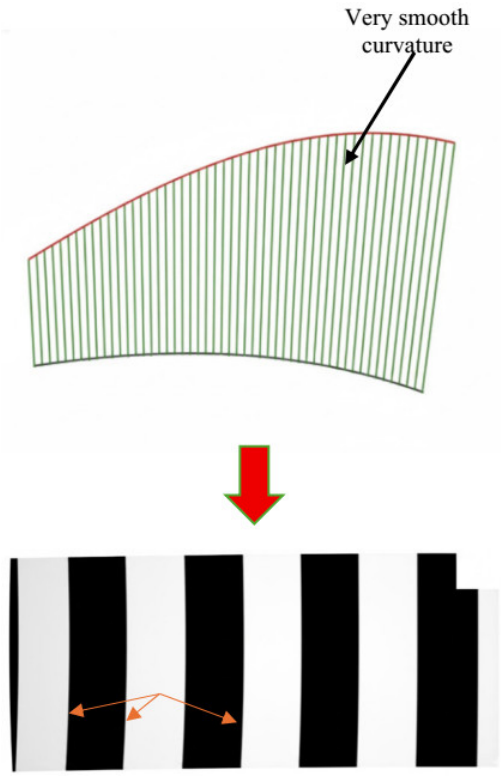

b)

Figure 14. Influence of high-frequency curvature oscillations on surface smoothness

A clear difference in surface quality can be readily observed through zebra reflection analysis. As shown in Figure 14(a), the surface generated from curves containing a high level of noise exhibits poor visual quality. This is manifested by distorted regions and irregular zebra flow patterns. In contrast, Figure 14(b) illustrates a surface characterized by a smooth curvature field, where the zebra stripes are continuous, uniformly distributed, and transition smoothly across the surface, resulting in a visually pleasing appearance.

This comparison highlights the critical role of curvature stability in surface reconstruction and demonstrates the advantage of employing Bézier curves in reverse engineering tasks that impose stringent aesthetic requirements.

Bézier curve representation and continuity conditions

In this study, the reconstructed curves are represented using fifth-degree Bézier curves, as illustrated in Figure 15. A quintic Bézier curve is defined as (28):

$$\mathrm{C}(t) = \sum_{i=0}^{5} \mathrm{P}_i \; B_i^5(t) = \sum_{i=0}^{5} \binom{5}{i} (1-t)^{5-i} t^i \mathrm{P}_i, t \in [0,1] \quad (28)$$

Curve joining and parametric continuity

In this work, two consecutive curve segments $P[t_0, t_1]$ and $Q[t_1, t_2]$, extracted from longitudinal sectional data of the rear bumper (Figure 12), are considered. These curves are first constructed to satisfy at least C^0 parametric continuity by enforcing coincidence of the terminal control point of the first curve and the initial control point of the second curve, i.e., $p_0 \equiv p_7$.

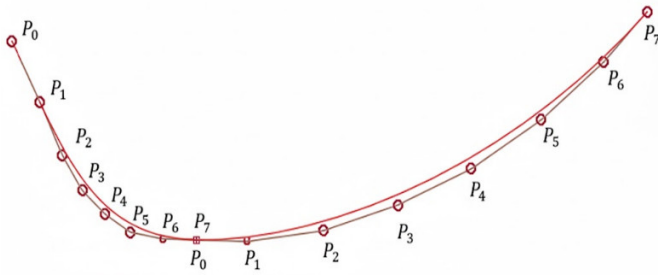

Figure 15. Two Bézier curve segments joined with parametric continuity

The two curves $P[t_0, t_1]$ and $Q[t_1, t_2]$ achieve C^1 continuity at the junction point $p_0 \equiv p_7$ if the following condition is satisfied (29):

$$\frac{3}{t_0 - t_1}(p_7 - p_6) = \frac{3}{t_2 - t_1}(p_1 - p_0) \quad (29)$$

This condition enforces equality of the first-order derivatives (tangent vectors) at the junction, both in direction and magnitude.

Finally, the curve pair satisfies G^2 continuity if G^1 continuity is achieved and the second-order derivatives are also matched (30):

$$\frac{6}{(t_0-t_1)^2}(p_7 - 2p_6 + p_5) = \frac{3}{t_2-t_1}(p_1 - p_0) \quad (30)$$

These continuity constraints are incorporated directly into the Lagrangian formulation or enforced as linear constraints within the optimization problem.

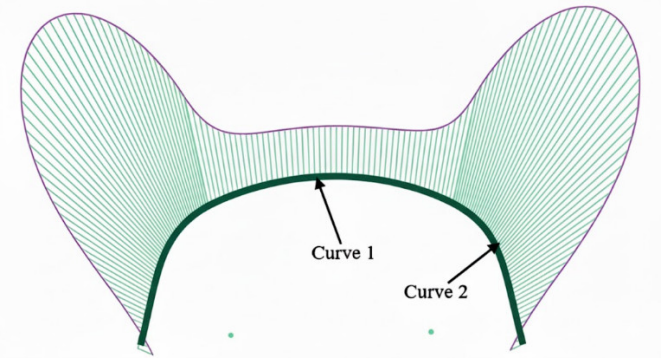

Figure 16. Bézier curves satisfying G^2 continuity

Figure 16 presents the curvature comb representation of the connected Bézier curve segments. The curvature combs are continuous and uniformly distributed along each segment, indicating smooth and stable curvature variation without localized oscillations caused by measurement noise. At the junctions between consecutive segments, no discontinuities or abrupt curvature changes are observed, confirming that high-order geometric continuity has been successfully maintained.

These results validate the effectiveness of the proposed approach in smoothing the initial noisy curves and establishing a reliable foundation for subsequent surface reconstruction.

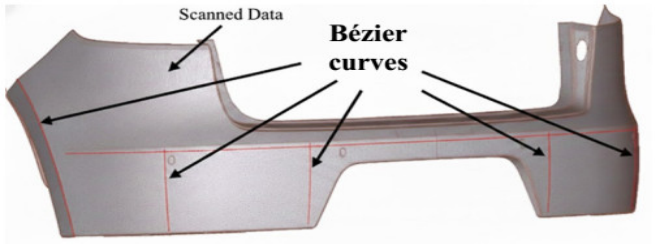

Figure 17. Reconstructed base-curve network derived from scanned data

Starting from the original scanned data, the proposed method identifies a complete set of Bézier curves required for surface generation, consisting of nine individual Bézier curves and one composite curve formed by connecting multiple Bézier segments (Figure 17). This base-curve network serves as the geometric backbone for the subsequent surface construction process.

3.3. Surface assessment

Based on the constructed network of Bézier curves, Bézier surface patches are generated through interpolation and blending between the boundary curves. Each patch is represented by a 5×5 control point grid, corresponding to a biquartic Bézier surface defined in both parametric directions. This representation provides sufficient degrees of freedom to accurately control the surface shape and the curvature distribution within each local region, while ensuring that the reconstructed surface directly inherits the geometric trends of the underlying curve network, particularly in transition areas with small radii of curvature.

The effectiveness of the optimization stage is evaluated using distance deviation maps between the reconstructed tensor-product Bézier surface and the original scanned data, as illustrated in Figures 18 and 19. Prior to optimization, the deviation distribution reveals several regions with errors exceeding ±0.15mm, which are mainly concentrated in areas characterized by high curvature fields and geometrically complex transitions. After applying the proposed optimization procedure, the deviation distribution is significantly improved: the proportion of surface area with deviations smaller than ±0.15mm increases markedly, while regions with larger deviations are reduced and become more uniformly distributed across the entire surface. These results demonstrate that the optimization step plays a crucial role in enhancing the geometric fidelity between the reconstructed surface and the original scan data.

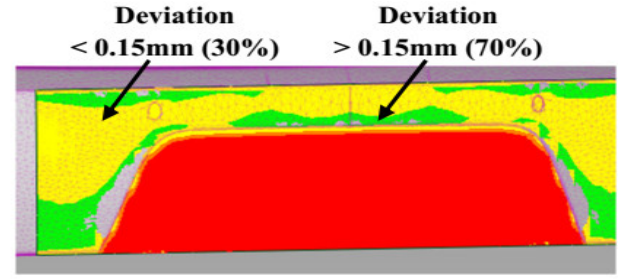

Before optimization

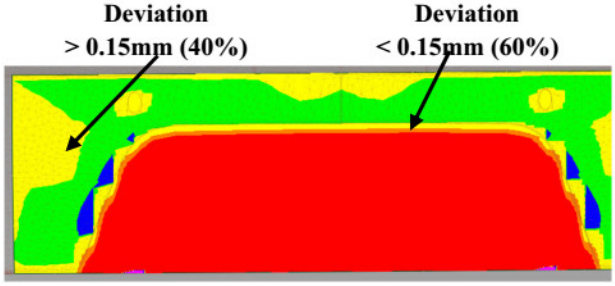

After optimization

Deviation

Figure 18. Post-optimization reconstruction result illustrating a close geometric agreement between the Bézier surface and the scanned data. The deviation map highlights regions of low error in green

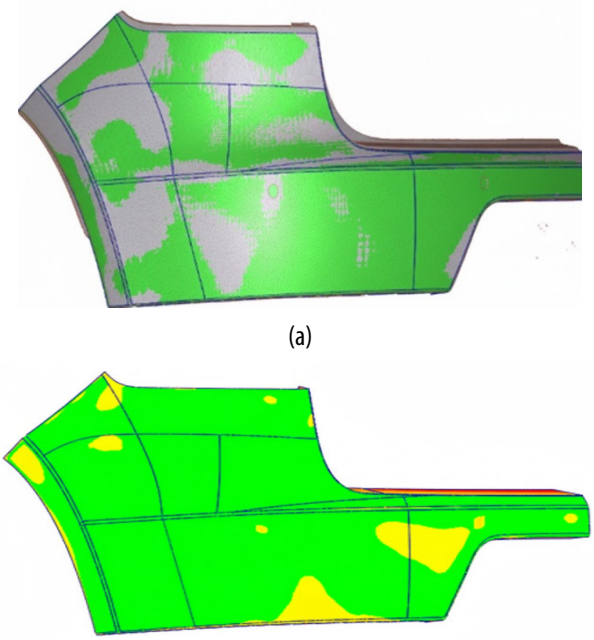

(a)

(b)

Figure 19. Error distribution between the reconstructed surface (b) and the original scanned data (a)

Table 2. Quantitative evaluation of surface fitting accuracy after Bézier reconstruction

Evaluation Parameter	Quantitative Metric	Acceptance Criterion	Conclusion
Root Mean Square (RMS) Error	0.087mm	< 0.2mm	Satisfies technical accuracy requirements
Maximum Deviation	0.18mm	< 0.2mm	Within the allowable tolerance range
Error Coverage	≈ 95% of surface area	< 0.15mm	Demonstrates high global fitting consistency

The quantitative indicators reported in Table 2 demonstrate that the reconstructed surface achieves high geometric accuracy. The RMS error is 0.087mm, and the maximum deviation is 0.18 mm, both of which fall within the targeted manufacturing tolerance. Furthermore, approximately 95% of the surface area satisfies $|\delta| < 0.15$mm, confirming that the reconstructed surface exhibits globally uniform and stable accuracy.

Qualitative evaluation. The aesthetic quality of the reconstructed surface is assessed by comparing the highlight flow between the original scanned data and the optimized surface. Figure 19 illustrates this comparison using Zebra analysis, which provides a visual assessment of surface smoothness and continuity.

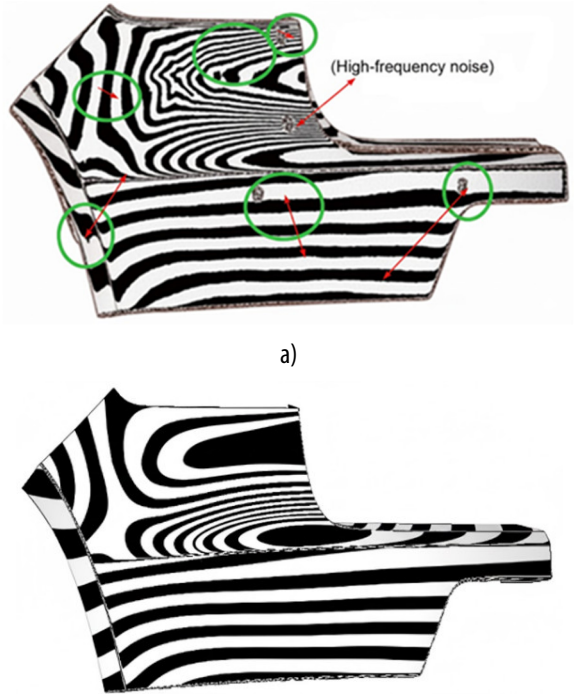

a)

b)

Figure 20. Comparison of the highline between the scanned data (a) and the reconstructed surface model (b) using Zebra analysis

Qualitative evaluation: The aesthetic quality of the reconstructed surface was assessed by comparing the highlight flow between the original scanned data and the optimized surface model. Figure 20 illustrates this comparison using Zebra analysis.

The Zebra analysis results in Figure 20 indicate:

Elimination of geometric defects: The reflection stripes on the raw scanned surface (Figure 20a) exhibit noticeable wrinkling and high-frequency oscillations caused by measurement noise. After variational optimization, these artifacts are completely removed, demonstrating that the reconstructed surface achieves a high level of optical smoothness.

Preservation of G^2 continuity: The reconstructed surface (Figure 20b) shows continuous and smoothly flowing Zebra stripes across patch boundaries, particularly in transition regions. This confirms that

curvature continuity constraints (G^2) are successfully enforced, ensuring smooth curvature variation and visually seamless surface transitions.

4. CONCLUSIONS

This study successfully developed an effective methodology for reconstructing high-curvature free-form surfaces from reverse engineering data. The proposed approach integrates curvature field analysis for objective morphological segmentation with variational optimization to tightly control both geometric accuracy and surface smoothness.

Specifically, the use of the Gaussian curvature field as the basis for automatic surface partitioning eliminates reliance on subjective, experience-based decisions. Meanwhile, the multi-objective variational formulation enables simultaneous optimization of data fitting accuracy and high-order geometric continuity (G^2). Experimental results demonstrate low reconstruction errors and uniform surface quality, confirming the robustness and effectiveness of the proposed method. Quantitatively, the method achieves an RMS error of 0.087mm and a maximum surface deviation of 0.18mm - both within the manufacturing tolerance of 0.2mm - with approximately 95% of the surface area exhibiting deviations below 0.15mm, demonstrating globally consistent and high-fidelity reconstruction performance.

Overall, the presented approach provides a systematic and highly automated framework for reconstructing complex free-form surfaces, meeting stringent engineering accuracy requirements while ensuring smooth and visually consistent surface behavior suitable for high-quality industrial applications.

However, the current study has several limitations that should be acknowledged. First, the proposed method was validated on a single automotive component (a rear bumper), and its generalizability to surfaces with more complex topological structures (e.g., multi-genus surfaces or surfaces with holes) has not yet been verified. Second, the computational cost of the variational optimization scales with mesh density, which may limit real-time applicability for large-scale datasets. Future research directions include: (i) extending the framework to handle multi-patch surfaces with arbitrary topology; (ii) incorporating deep learning-based point cloud segmentation to further automate patch layout determination; and (iii) investigating GPU-accelerated implementations to improve computational efficiency for industrial-scale applications.

REFERENCES

[1]. S. Dumortier, B. Falcidieno, C. Pienovi, "Reverse engineering of free-form surfaces," *Computer-Aided Design*, 29, 2, 135-142, 1997. https://doi.org/10.1016/S0924-0136(97)00340-3

[2]. A. Q. Lin, Y. X. He, "Research Based on Reverse Engineering Technology of Complex Structure Product," *Applied Mechanics and Materials*, 741, 806-809, 2015. Available: https://www.scientific.net/AMM.741.806

[3]. H. Tsuchie, K. Yamamoto, S. Kanai, "Interpretation of clay modeling using differential geometry and its application to surface reconstruction," *Engineering with Computers*, 41, 2431-2441, 2025. https://doi.org/10.1007/s00366-025-02111-5

[4]. J. Hu, X. Zhong, "PDE-based surface reconstruction in automotive styling design," *Multimedia Tools and Applications*, 82, 1185-1202, 2023. https://doi.org/10.1007/s11042-022-12487-9

[5]. Y. Huang, X. Qian, "Dynamic B-spline surface reconstruction from unorganized point clouds," *Computer-Aided Design*, 39, 9, 804-814, 2007. https://doi.org/10.1016/j.cad.2007.06.008

[6]. Q. Wang, J. X. Li, Y. L. Ke, "Deformation-based freeform feature reconstruction from measured data," *Journal of Zhejiang University - Science A*, 9, 6, 781-789, 2008. https://doi.org/10.1631/jzus.A0820244

[7]. L. Zhang, C. Xiong, J. Tang, "Research on curved surface reconstruction based on Geomagic Design X," *Topics in Chemical & Material Engineering*, 2, 1, 77-82, 2023. https://jglobal.jst.go.jp/en/public/202502239332732427

[8]. K. Otto, K. Wood, *Product Design: Techniques in Reverse Engineering and New Product Development*. Upper Saddle River, NJ, USA: Prentice Hall, 2001.

[9]. G. Farin, *Curves and Surfaces for Computer-Aided Geometric Design*, 5th ed. San Diego, CA, USA: Academic Press, 2002.

[10]. M. E. Mortenson, *Mathematics for Computer Graphics Applications*, 2nd ed. New York, NY, USA: Industrial Press, 1999.

[11]. V. Raja, K. J. Fernandes, *Reverse Engineering: An Industrial Perspective*. London, U.K.: Springer, 2008. https://doi.org/10.1007/978-1-84628-856-2

[12]. M. Berger, J. A. Levine, B. T. Smith, "Curvature-based segmentation of point clouds for surface reconstruction," *Applied Geomatics*, 1, 3, 123-135, 2009. Available: https://link.springer.com/article/10.1007/s12518-009-0002-4

[13]. T. Kalker, "Clay modelling - from sketch to model," *ATZ Worldwide*, 117, 4, 50-55, 2015. https://doi.org/10.1365/s40112-015-1004-8

[14]. Autodesk Inc., *Autodesk Alias - Help & Documentation*. 2021. Available: https://www.autodesk.com/products/alias

[15]. Z. Huang, Y. Wen, Z. Wang, J. Ren, K. Jia, "Surface reconstruction from point clouds: A survey and a benchmark," *arXiv:2205.02413*, 2022. Available: https://arxiv.org/abs/2205.02413

[16]. R. Sulzer, R. Marlet, B. Vallet, L. Landrieu, "A survey and benchmark of automatic surface reconstruction from point clouds," *arXiv:2301.13656*, 2023. Available: https://arxiv.org/abs/2301.13656

[17]. Z. Zhu, et al., "PDE patch-based surface reconstruction from point clouds," *Journal of Computational Science*, 61, 101647, 2022. https://doi.org/10.1016/j.jocs.2022.101647

[18]. Y. Liu, A. Obukhov, J. D. Wegner, K. Schindler, "Point2CAD: Reverse engineering CAD models from 3D point clouds," in *Proc. IEEE/CVF Conf. Computer Vision and Pattern Recognition (CVPR)*, 3763-3772, 2024. https://doi.org/10.1109/CVPR52733.2024.00361